RSC Advances

ROYAL SOCIETY OF CHEMISTRY

www.rsc.org/advances

Journal Name

ARTICLE

A Low-Temperature Sintered Heterostructure Solid Film of Coordination Polymer Nanoparticles: An Electron-Rectifier Function Based on Partially Oxidised/Reduced Conductor Phases of Prussian Blue

Received 00th January 20xx,
Accepted 00th January 20xx

DOI: 10.1039/x0xx00000x

www.rsc.org/

Kenta Ono, Manabu Ishizaki,* Shinobu Soma, Katsuhiko Kanaizuka, Takanari Togashi and Masato Kurihara*

Inks of surface-modified nanoparticles (NPs) are a promising fluid for fabricating thin-film electronic devices; however, such NPs are still functionally discrete from each other. Therefore, reconstituting electronic communication among the NPs has been a challenging subject for their nanoscale interfacial assembly. Here, we demonstrate the reconstitution (sintering) ability of surface-modified Prussian blue (PB) and its Ni-replaced analogue (Ni-PBA) NPs that leads to multilayer electronic functions. A double-layer (DL) rigid solid film of the PB (bottom layer) and the Ni-PBA (top layer) NPs has been successfully fabricated on indium-tin-oxide (ITO) substrates by a spin-coating technique using their water inks and a low-temperature sintering process between 120 and 150 °C to immobilise the spin-coated NPs without serious mismatch on the heterostructure DL interface. The DL solid films act as an electron-rectifier device, which is entirely characterised by a PB bottom layer with a minimum nanoscale thickness of ~20 nm. In the mechanism of the electron-rectifier phenomenon, we reveal the appearance of theoretically predicted partially oxidised/reduced conductor phases of PB.

Introduction

Coordination polymers (CPs) are well-known high-performance functional crystals,[1,2] and innumerable CP crystals have been synthesised *via* various types of infinite bonding chains composed of metal ions and organic/inorganic bridging molecules. Prussian blue (PB), $Fe^{III}_4[Fe^{II}(CN)_6]_3 \cdot xH_2O$, is a historic blue pigment and the first artificial CP crystal with lattice spaces surrounded by mixed-valence Fe(II)-CN-Fe(III) 3-D frameworks (Fig. 1a).[3] So far, PB and its metal-replaced analogue (PBA) crystals have been intensively investigated as a representative CP family that shows versatile functionalities such as electronic, photonic, magnetic, and their hybridization.[2,4-7] In particular, the inherent natures originating from the extended *d*-π electron bonding networks throughout the crystals are anticipated to be advantageously utilised to create a new class of thin-film device functions. Actually, from the advent of electro-deposited PB and PBAs,[5-7] the crystalline thin film specifically shows electrochemically reversible redox couples on electrodes, *e.g.,* Fe(II)-CN-Fe(II) (Prussian white (PW)) ↔ Fe(II)-CN-Fe(III) (PB) and PB ↔ Fe(III)-CN-Fe(III) (Prussian yellow (PY)). These redox states include fascinating spin-conjugated electronic properties for PB-based electronic/spintronic devices[4]; however, electro-deposition technology generally contains inconvenient processability for the industrial and scientific production of various types of thin-film devices.

Currently, the importance of printed electronics (PE) for producing electronic devices using various substrates has increased globally because such solution-based technology with higher processability strongly contributes to a low-consumption industry with respect to saving energy, resources, and time.[8-12] Inks and pastes of surface-modified nanoparticles (NPs) are promising candidates for printable fluids; nevertheless, NPs are in a functionally discrete state from each other. Therefore, reconstituting electronic communication among such discrete NPs on substrates has been a scientifically challenging subject for their nanoscale interfacial assembly.[7,9-12] In addition, the low-temperature reconstitution *via* sintering among the NPs at ≤ 150 °C is an indispensable technique to realise flexible and/or lightweight thin-film electronic devices using heat-sensitive commodity plastic substrates such as polyethylene terephthalate (PET).[9,13] Metal NPs of silver and copper have been widely adopted for printed conductive circuits. Their low-temperature sintering caused by the melting-point drop phenomenon occurs even at room temperature,[9-11,15] whereas a similar phenomenon is intrinsically unavailable in the case of CPs due to the poor mobility of surface atoms, even with the nanoscale downsizing of their crystals.

Yamagata University, 1-4-12 Kojirakawa-machi, Yamagata, 990-8560 Japan.
† Footnotes relating to the title and/or authors should appear here.
Electronic Supplementary Information (ESI) available: [details of any supplementary information available should be included here]. See DOI: 10.1039/x0xx00000x

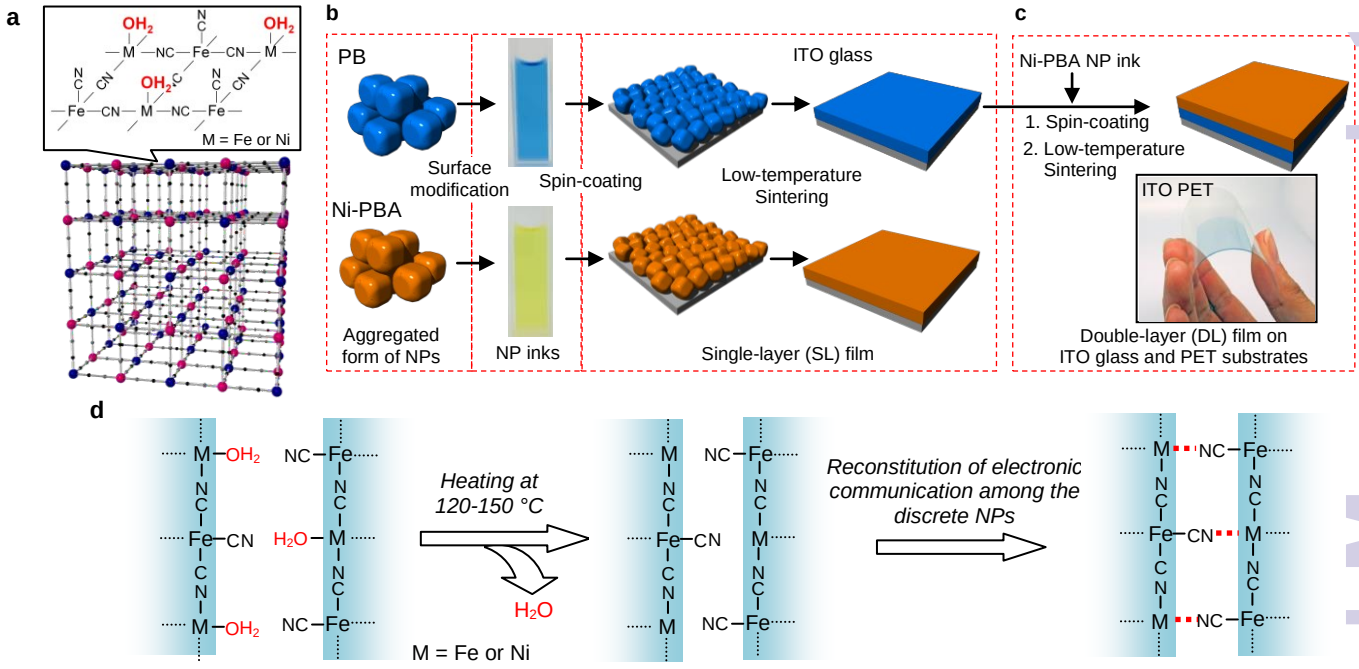

Fig. 1. (a) A cyano-bridged coordination polymer (CP) structure of PB and Ni-PBA. Schematic experimental procedures for (b) single-layer (SL) and (c) double-layer (DL) spin-coated films of the PB and Ni-PBA NPs using their dispersion solutions (inks) on ITO glass and PET substrates. The curved DL film on the ITO PET substrate exhibits (photograph) a transparent blue color because of the intense photo-absorption coefficient of PB. (d) A proposed mechanism for low-temperature sintering among the discrete PB and Ni-PBA NPs.

In a series of reports, we have focused on greener synthetic methodologies of PB and PBA NPs suitable for industrial applications.[16,17] In conventional synthesis, PB has been obtained as an insoluble solid immediately precipitated from a concentrated aqueous mixture of $Fe^{3+/2+}$ and $[Fe^{II/III}(CN)_6]^{4-/3-}$. We have introduced the conclusion that the insoluble PB solid is a physically aggregated form of ~10-nm NPs,[16,17] and noticed that in the surface active reaction sites of each PB NP, the 3-D network with cyano-bridged *d*-π bonding is discontinuous, and each PB NP inevitably bears active surface reaction sites of Fe^{III}-OH_2 (Fig. 1a).[16,17] By partially modifying the surface reaction sites using $[Fe(CN)_6]^{4-}$ (Fig. S1), PB NPs can be stably redispersed into water directly from the insoluble PB solid to prepare a dense PB NP ink. Dense water inks of PBA NPs have been prepared using a synthetic strategy similar to PB. Furthermore, a low-temperature sintering method suitable for the partially surface-modified PB and PBA NPs has been developed whose mechanism is completely different from the melting-point drop of metal NPs.[9-11,15]

In this study, we demonstrate high-processability features focusing on PB and PBA NP inks, to construct high-performance multilayer solid thin films[18] (Fig. 1): (1) single-layer (SL) thin films are prepared on various substrates by a simple spin-coating solution process (Fig. 1b); (2) a low-temperature heating process transforms the spin-coated film of the NPs into a densely packed rigid solid film *via* our proposed sintering mechanism (Fig. 1d); (3) heterostructure multilayer thin films of the NPs with different metal compositions can be produced by combination of successive spin-coating and low-temperature sintering (Fig. 1c). Here, we construct low-temperature sintered heterostructure double-layer (DL) films on indium-tin-oxide (ITO) glass and PET substrates (Fig. 1c, photograph) using water inks of the PB NPs and its Ni-replaced analogue (Ni-PBA) NPs. The film thickness is successfully adjusted in nanoscale, depending on the concentrations of their NP inks. The as-prepared DL rigid solid films composed of the PB (bottom layer) and the Ni-PBA (top layer) NPs exhibit an electron-rectification phenomenon[19] which is controlled by the nanoscale thickness of the bottom PB layer. An essential question still remains as to why the PB insulator phase[20] can transport holes/electrons from the electrodes to change into the PY/PW phase. Our elucidation of the electron-rectification mechanism will shed light on the long-standing question regarding the theoretically predicted half-metallic conductivity of the partially oxidised/reduced PB phases, *i.e.*, hole-/electron-injected PB phases.[21]

Results and discussion

Characterisation of PB and Ni-PBA NP solids and inks

Scherrer's particulate sizes of the insoluble PB and Ni-PBA NP solids prepared by conventional synthesis were estimated to be 8.9 and 13 nm, respectively, based on the half-height widths of significantly broadening powder X-ray diffraction (XRD) signals (Fig. S2). According to the fluorescent X-ray (XRF) analysis, the metal composition ratio of the insoluble Ni-PBA NP solid was estimated to be Fe:Ni = 1:1.43. The metal composition ratio deviates slightly from the ideal ratio of Fe:Ni = 1:1.5 ($Ni_3[Fe(CN)_6]_2$), and the deficient positive charge is compensated by potassium ions as a formula of $K_{0.28}Ni_{2.86}[Fe(CN)_6]_2$, in accordance with earlier reports.[16] PB

and Ni-PBA NPs were well dispersed into water by partial displacement between H_2O and $[Fe(CN)_6]^{4-}$ on the surface sites of Fe(III) (Fig. S1), and number-averaged dynamic light-scattering (DLS) particle sizes in their inks were 17 ± 5 and 49 ± 26 nm, respectively (Fig. S3b), indicating that the NPs were partially aggregated as secondary particles dispersible in water. The zeta potentials of the PB and Ni-PBA NPs measured in their diluted water inks were -32 and -35 mV, respectively. The NPs underwent surface modification with $[Fe(CN)_6]^{4-}$ and were allowed to be dispersed in water by their mutual electrostatic repulsion due to negative surface charges.[16] In transmission electron microscopy (TEM) images (Fig. 2a), the surface-modified PB and Ni-PBA NPs were distributed at 8.3 and 12 nm in mean dimensions, respectively, and lattice images of each NP were observed in the high-resolution TEM (Fig. S3a). As a result, the diluted PB and Ni-PBA NP inks exhibited high transparency of blue and yellow colours with the absorption maximal wavelength, λ_{max} = 683 and 394 nm, respectively (Fig. S3c).

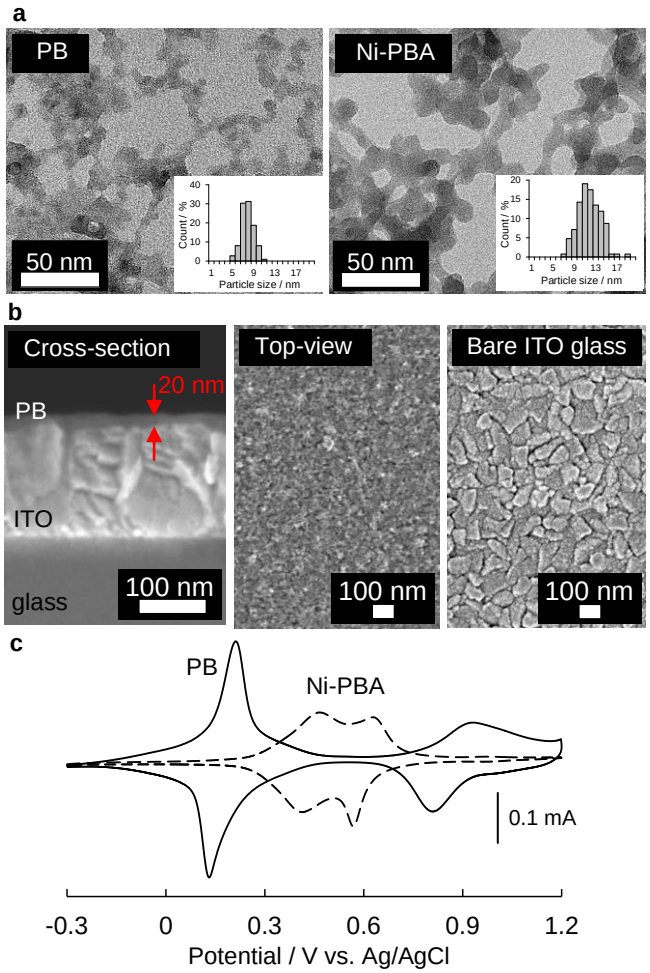

Fig. 2. (a) TEM images of the PB and Ni-PBA NPs, where the dilute NP inks were dropped on TEM grids. (b) FE-SEM cross-section and top-view images of the low-temperature sintered film with a 20-nm thickness of PB NPs at 150 °C, and a top-view image of the bare ITO glass substrate. (c) Cyclic voltammograms of the sintered single-layer (SL) solid films of PB and Ni-PBA NPs in a 0.1 M KCl aqueous solution controlled at pH 3. Scan rate is 100 mV/s.

Characterisation of PB and Ni-PBA films

Inks of the PB NPs could be uniformly spread on indium-tin-oxide (ITO) glass substrates by simple spin-coating (Fig. 1b). Coated NP films were scratched by atomic force microscopy (AFM) probes; the NP images became obscure in the first contact-mode scan (Fig. S4a), and the scanning area of the film surface was extensively scratched by the AFM probe within the third scan (Fig. S4b). This scratch test suggests that spin-coated NP films are essentially fragile. To overcome the fatal fragility of the NP films, a low-temperature sintering process has been adopted to create new chemical bonds among the NPs.[17] We have focused on active coordination sites exposed on the surface of each PB and PBA NP, in which the 3-D network of metal-cyano-bridged *d*–*π* bonds is discontinuous (Fig. 1a). The active surface sites, $M–OH_2$ (M = Fe^{III} or Ni^{II}), are allowed to be modified by the addition of $[Fe^{II}(CN)_6]^{4-}$ to generate $M–[NC–Fe^{II}(CN)_5]^{4-}$ moieties on the NP surfaces.[17] To achieve low-temperature sintering among NPs, a partial surface modification has been performed. In this study, 70% of the surface $M–OH_2$ sites are covered with $[Fe^{II}(CN)_6]^{4-}$ as an ideal cubic NP dimension of 10 nm (Fig. S1). The partially surface-modified NPs had a potential ability to connect to each other in the spin-coated films; functionally discrete NPs are allowed to connect *via* a new metal-cyano-bridged *d*–*π* bonding network of $M–[NC–Fe^{II}(CN)_4–CN]^{4-}–M$ from $M–[NC–Fe^{II}(CN)_5]^{4-}$ and $M–OH_2$ with the release of H_2O ligands (Fig. 1d).

Based on the thermogravimetric (TG) weight loss, the coordination and crystal water molecules of the PB and Ni-PBA NPs were released at between 50 and 200 °C (Fig. S5). The 3-D framework structure of the NPs was maintained against heating of up to 150 °C because the powder XRD pattern was unchanged after heating (Fig. S2).[22] Through the heating process at 150 °C or lower, the spin-coated films of the PB NPs adhered well to the ITO substrates. The fragility of the films was surprisingly improved; low-temperature sintered film with a thickness of approximately 20 nm sustained almost no damage under the same AFM contact-mode scanning conditions as compared with the spin-coated films before sintering (Fig. S4). In addition, PB NPs were densely packed throughout a similarly sintered film with a 340-nm thickness without any serious voids or cracks from the scanning electron microscopy (SEM) cross-section image (Fig. S6). The fragility of the spin-coated Ni-PBA NP films was similarly improved by heating at 150 °C or lower. The densely packed Ni-PBA NPs were observed in the SEM cross-section image (Fig. S6), and the Ni-PBA NP film with a 410-nm thickness was robust based on the AFM scratch test (Fig. S7). As a result, the PB and Ni-PBA NPs apparently never re-eluted into water from the rigidly sintered films on the ITO substrates.

Electrochemical properties of PB and Ni-PBA NP films

The as-sintered PB NP films showed characteristic reversible redox properties in their cyclic voltammograms (CVs) (Fig. 2c).[5] The K^+ ions size-selectively contributed to the reversibility to afford two sharp CV redox wave couples at $E_{1/2}$ = 0.16 and 0.84 V of PW ↔ PB ↔ PY. The redox response occurred selectively

in cations (Fig. S8). The Stokes radii fit better with the crystal lattice spaces of PB in the order of K^+ >> Na^+ > Li^+.[5] In the sintered film of the spin-coated Ni-PBA NPs, the CVs were also influenced by the counter cations (Fig. S8). The redox waves were essentially derived from Fe^{III}-CN-Ni^{II} ↔ Fe^{II}-CN-Ni^{II}, while two divided redox couples at $E_{1/2}$ = 0.44 and 0.60 V were apparently observed in the case of the K^+ ions (Fig. 2c). The division is probably caused by the different surroundings of Fe^{III}-CN-Ni^{II} moieties due to their defect sites, *i.e.*, sites deficient in $[Fe^{III}(CN)_6]^{3-}$. The redox potentials between Fe^{III}-CN-Ni^{II} ↔ Fe^{II}-CN-Ni^{II} were negatively shifted in the order of Li^+ ≈ Na^+ > K^+.

The relationship between the thickness of sintered films and the concentrations of PB and Ni-PBA NP inks was investigated using a stylus profiler (Fig. S9). The sintered films are adjustable from ten or several tens of nanometres over a submicrometre range of thickness by simple spin-coating techniques. Under the present conditions, the thickness of PB and Ni-PBA NP films was almost linearly controlled up to 100 and 250 nm, respectively, depending on the concentrations of the NPs. The deviation from linearity in the high concentration range is probably caused by complicated factors such as increased viscosity related to thixotropy.

In preparing the DL films, the Ni-PBA NP ink was spin-coated on the sintered bottom layer of the PB NPs on ITO (Fig. 1c), and the as-hybridised films were further sintered. In a typical case, the top layer was formed with a thickness of ~150 nm on the bottom layer with a thickness of ~20 nm (Fig. S10). The heterostructure DL film exhibited an intriguing electronic property (Fig. 3a) that was definitely different from those of the single-layer (SL) films (Fig. 2c). In the CVs of the DL films, two reversible redox couples appeared at the same applied potentials, $E_{1/2}$ = 0.16 and 0.84 V, as those of the PB SL film. A new rectified current couple was observed at E_{pa} = 0.80 and E_{pc} = 0.16 V. The redox couples at the potentials, $E_{1/2}$ = 0.44 and 0.60 V, derived from the SL film of Ni-PBA NPs disappeared in the DL film. To elucidate the evolution mechanism of the rectification phenomenon, the thickness dependency of its bottom and top layers was investigated. The bottom layer was formed by two different thicknesses of 10 and 20 nm using adjusted concentrations of the PB NP ink, and then the Ni-PBA layer was overlaid at a constant thickness of ~150 nm. The redox currents at $E_{1/2}$ = 0.16 and 0.84 V were increased by thickening the bottom layer (Fig. 3a); therefore, the two redox couples were attributed to the electron transfer between the PB layer and the ITO electrode. The rectified current couple became obscure in the case of the 10-nm thickness. The rectified peak current intensities (i_{pa} and i_{pc}) depended on the thickness of the top layer fabricated on the 20-nm bottom layer (Fig. 3b), indicating that the rectified charge density of the DL films can be accumulated as the top layer increases in thickness. The rectification response of the DL film appeared more clearly in the case of K^+ than in Na^+ and Li^+ (Fig. 3c). When the 20-nm bottom layers were sintered at 100 °C, the electron-rectification phenomenon resulted in the appearance of weak leak currents in the CV (Fig. S11). This is probably caused by incomplete connections (incomplete sintering) among the bottom PB NPs. If the bottom and top layers were heated to between 120 and 150 °C, the rectification phenomena could be reproducibly observed (Fig. S11). These results imply that the top layer electrochemically united with the bottom layer *via* the low-temperature

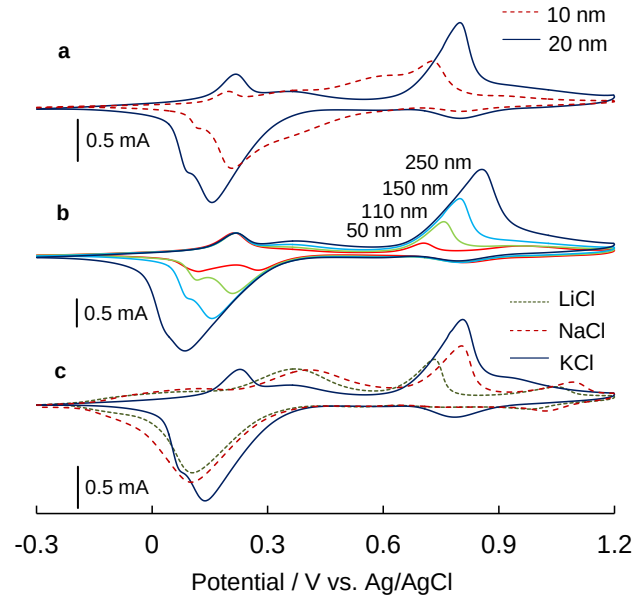

Fig. 3. Electron-rectification properties of the low-temperature sintered double-layer (DL) films of the PB (bottom layer) and Ni-PBA (top layer) NPs on ITO glass substrates in a 0.1 M KCl aqueous solution controlled at pH 3. (Scan rate is 100 mV/s.) (a) Cyclic voltammograms of the DL films of a Ni-PBA layer with a 150-nm thickness and a PB layer with two different thicknesses, 10 and 20 nm. (b) Cyclic voltammograms of the DL films of a Ni-PBA layer with increased thicknesses from 50 to 250 nm and a PB layer with a constant 20-nm thickness. (c) Cyclic voltammograms of a Ni-PBA layer with a 150-nm thickness and a PB layer with a 20-nm thickness in an aqueous solution of LiCl or NaCl instead of KCl.

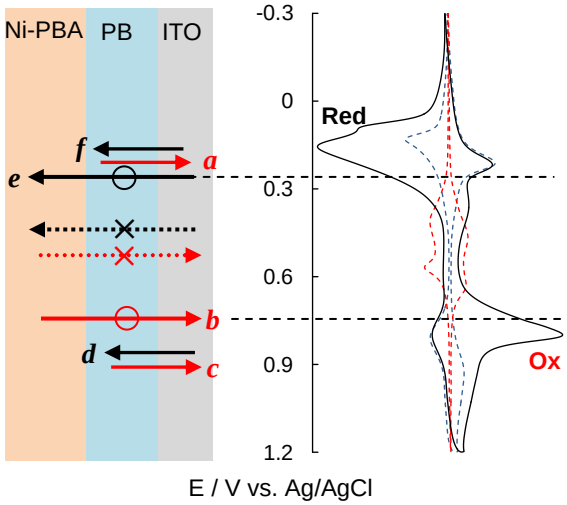

Fig. 4. A proposed mechanism of the rectification phenomenon of the DL film. Cyclic voltammograms of the DL, the PB SL, and the Ni-PBA SL films are shown by black solid, blue broken, and red broken lines, respectively.

reconstitution of the electron-transferable *d–π* bonding networks among the NPs. The bottom layer of the sintered PB NPs behaves as a high-performance blocking (insulator) solid layer for electron transfer synchronised with K^+ migration between the ITO electrode and the top layer.

Electron-rectification mechanism and partially oxidised/reduced conductor phases of PB

In the rectification phenomenon, the redox sequence of potentials ***a*** to ***f*** is shown in Fig. 4; the bottom layer is oxidised from PW to PB at potential ***a***, corresponding to the redox couple PW ↔ PB of the PB SL film. The Fe^{II}-CN-Ni^{II} state cannot be oxidised to the Fe^{III}-CN-Ni^{II} state up to a starting potential, ***b***, for oxidation from PB to PY, meaning that the PB state of the bottom layer closes the electron-transfer pathway between the top layer and the electrode as an insulator. At the starting potential, ***b***, *i.e.*, the negative potential edge of the redox wave of PB ↔ PY, the bottom layer can open the electron-transfer pathway for the top layer. Thus, the oxidation current flow from the top layer to the electrode is observed around potential ***b*** as the rectification phenomenon. The redox wave of PB ↔ PY appears at the same potentials, ***c*** and ***d***, as in the PB SL film. In the reverse potential scan from ***d*** to ***f***, the Fe^{III}-CN-Ni^{II} state is not subject to reduction to Fe^{II}-CN-Ni^{II} up to the starting potential, ***e***, for the reduction from PB to PW. At the starting potential, ***e***, *i.e.*, the positive potential edge of the redox wave of PB ↔ PW, the bottom layer can open the electron transfer pathway for the top layer. The rectification current flow from the electrode to the top layer is observed around potential ***e***. The redox wave of PB ↔ PW appears at the same potentials, ***a*** and ***f***, as in the PB SL film.

According to the proposed mechanism (Fig. 4), three different phases appeared in the bottom PB layer within the potential window between the two redox couples corresponding to PW ↔ PB (***a*** and ***f***) and PB ↔ PY (***c*** and ***d***). The bottom PB layer initially behaves as an insulator phase within potentials ***e*** and ***b***. If some electrons and holes are injected into the PB insulator layer near potentials ***e*** and ***b***, respectively, they are allowed to migrate from the ITO electrodes into the top Ni-PBA layer. After the completion of the redox reaction, *i.e.*, electron and hole accumulation of the Ni-PBA layer, the redox state of PB can be changed into PW and PY. These results strongly indicate that the PB insulator layer is transformed into partially oxidised/reduced conductor phases, *i.e.*, hole-/electron-injected conductor phases.

In 2009, Illas *et al.* predicted by the periodic density function calculation that PY and PW behave as half-metals.[21] In the PB oxidation process to PY, the Fermi level was gradually stabilised into the topmost occupied band due to the t_{2g} orbital electrons. A partially oxidised form, $(K_{0.75}Fe[Fe(CN)_6] = K_{0.75}Fe^{III}[Fe^{III}(CN)_6]_{0.25}[Fe^{II}(CN)_6]_{0.75})$, of PB ($KFe^{III}[Fe^{II}(CN)_6]$) theoretically exhibited a very limited electron density at the Fermi level, and the top of the conduction band is less than 0.05 eV above it. In the subsequent oxidation of the PB to PY, the top of the conduction band changed linearly within a range of 0.05 and 0.75 eV. In 2011, Einaga *et al.* synthesised PB and its partially oxidised form, Berlin green (BG) powders, and they concluded on the basis of the experimental conductivities and theoretical calculations that PB was reaffirmed as a bar[illegible] insulator and BG as a conductor.[20] The previously mentioned theoretical and experimental results about the partially oxidised form of PB bearing a half-metallic nature a[illegible] consistent with our mechanism for this rectification phenomenon.

Electrochemically or synthetically obtained films of the PW state are unstable and return to the PB state.[23] Therefore, the theoretically predicted half-metallic nature of partially reduced PB states is experimentally unclear. In addition, the reduction process from PB to PW is more theoretically complicated than that from PB to PY because of the large changes involved in the structural (lattice expansion) and electronic properties in the former process.[21] In this study, we have successfully obtained experimental evidence that the partially reduced state of PB is defined as a conductor phase electro[illegible] transferable into the Ni-PBA top layer from the ITO electrode.

Conclusions

With progress in the miniaturisation of electronic devices, the functional units are anticipated to become increasingly smaller. Therefore, molecule-[10,13,21] and NP-based[25] electronic devices have been competitively developed for actual applications. From the perspective of an NP-based technology, the electron-rectifier device can be entirely characterised by a bottom layer with a minimum thickness of approximately 20 nm, that is, a stack layer of only two or three PB NPs. In the SEM cross-section image (Fig. 2b), the sintered PB NPs are uniformly adhered as a film of approximately 20-nm thickness on the ITO granular layer, and the film surface is surprisingly flat against the roughness of the ITO substrate. In the SEM top-view image, the PB NPs homogeneously cover the ITO granular surface (Fig. 2b) without any serious inter-particulate gaps or vacant domains. The low-temperature sintering successfully prevents the functional disorder of the bottom stack layer of two or three PB NPs when the Ni-PBA NP inks are overlaid. In fact, cracks due to mismatches in the DL heterostructure interface are never observed in the film adhered to the ITO substrate in the SEM cross-section image of the electron-rectifier film (Fig. S10). In a preliminary attempt to produce PE devices using heat-sensitive commodity plastics and solid films of CP NPs, DL films are successfully prepared on an ITO substrate made of PET, and it reproduces a similar electrochemical response due to electron rectification on the curved substrate, which demonstrates its flexibility (Fig. 1c, S12).

In the electro-rectification phenomenon, we can experimentally visualise both of the partially oxidised/reduced conductor phases along with an insulator phase in the PB NP solid film within its redox-potential window. The conductor phases are a new class for designing PB- and PBA-based electronic and spintronic devices. Inks of surface-modified NPs are advantageously available as a printable fluid; nevertheless, the NPs are in a functionally discrete state from each other. Reconstituting electronic communication among the discrete NPs will be a key technology in CP electronics (Fig. 1d). For

future applications, further investigations of the low-temperature sintering (reconstitution) processes among CP NPs will lead to a variety of high-performance printed electronic/spintronic devices that originates from the extended d–π bonding networks.

Experimental

Materials

Guaranteed-grade $Fe(NO_3)_3{\cdot}9H_2O$, $Ni(NO_3)_2{\cdot}6H_2O$, $K_4[Fe(CN)_6]{\cdot}3H_2O$, and $K_3[Fe(CN)_6]$ and extra-pure grade $Na_4[Fe(CN)_6]{\cdot}10H_2O$ were purchased from Kanto Chemicals. All reagents used to prepare the insoluble PB and Ni-PBA NP solids were used without further purification. Guaranteed-grade LiCl was supplied from Nacalai Tesque. Guaranteed-grade NaCl and KCl were supplied by Kanto Chemicals. ITO glass (10 Ω/sq.) and ITO PET (60 Ω/sq.) substrates were purchased from Furuuchi Chemical and Sigma-Aldrich, respectively.

Apparatuses

Powder X-ray diffraction (XRD) analyses were performed using a Rigaku MiniFlex II desktop X-ray diffractometer (Cu $K\alpha_1$ radiation). The metal compositions of the Ni-PBA NPs were determined by fluorescent X-ray (XRF) analyses using a Rigaku Primini wavelength dispersive X-ray spectrometer. The dynamic light-scattering (DLS) particle sizes and the zeta potentials of the PB and Ni-PBA NPs were measured on an Otsuka ELSZ-1000ZS particle-size analyser. Thermogravimetric analysis (TG) was performed using a TA Instruments SDT Q600 under a stream of He, and the liberated gasses from the PB and Ni-PBA NPs synchronised with the TG weight loss were analysed using a JEOL JEM-Q1050 mass spectrometer. Thermogravimetric-differential thermal analysis (TG-DTA) was performed using a Rigaku Thermo plus EVO2 under a stream of air. Spin-coated thin films were fabricated on ITO glass and ITO PET substrates using Mikasa MS-A100 and Kyowa Riken K359 S-1 spin-coaters, respectively. The thicknesses of spin-coated and low-temperature sintered films of the PB and Ni-PBA NPs were determined using a Bruker Dektak XT stylus profiler. Scanning electron microscope (SEM) and transmission electron microscope (TEM) images were recorded on a JEOL JSM-7600F and JEOL JEM-2100F, respectively. The fragility of the NP film surfaces was evaluated by probe scratching *via* contact-mode images of atomic force microscopy (AFM) using a Shimadzu SPM-9700 scanning probe microscope. An ALS electrochemical analyser, model 1100P, was used to measure the cyclic voltammetry. ITO glass and ITO PET substrates were plasma treated using Meiwafosis SEDE.

Preparation of PB NP inks

The insoluble PB NP solid was prepared in accordance with the previous literature.[16] An aqueous solution (7.50 mL) of $Fe(NO_3)_3{\cdot}9H_2O$ (3.23 g, 8.00 mmol) was added to an aqueous solution (12.0 mL) of $Na_4[Fe(CN)_6]{\cdot}10H_2O$ (2.90 g, 6.00 mmol). The reaction mixture was vigorously stirred for 30 min. The resulting blue precipitate of PB was centrifuged at 2740 × g for 10 min, washed with water three times and with methanol once, and dried under reduced pressure. The as-obtained insoluble PB NP solid with a yield of 1.84 g (84%) was $Fe^{III}_4[Fe^{II}(CN)_6]_3{\cdot}xH_2O$ (x = 10–15) in the formula, where the number of waters of crystallization, x, was determined using TG-DTA.

The insoluble PB NP solid (1.53 g, 1.40 mmol as a formula of $Fe^{III}_4[Fe^{II}(CN)_6]_3{\cdot}13H_2O$) was stirred with water (10 mL) for 30 min. Into the resulting blue suspension, an aqueous solution (10 mL) of $K_4[Fe(CN)_6]{\cdot}3H_2O$ (0.414 g, 0.980 mmol, 10% based on the total number of Fe ions of the PB) was added, and the mixture was then stirred for 2 days. After centrifugal removal of aggregated large particles of the PB NPs at 2600 × g for 10 min, the ink of the PB NPs (68.2 mM as the formula of $Fe^{III}_4[Fe^{II}(CN)_6]_3{\cdot}13H_2O$) was diluted with water to adjust to various concentrations.

Preparation of Ni-PBA NP inks

The insoluble Ni-PBA NP solid was prepared in accordance with previous studies.[16] An aqueous solution (12 mL) of $Ni(NO_3)_2{\cdot}6H_2O$ (3.49 g, 12.0 mmol) was added to an aqueous solution (24 mL) of $K_3[Fe(CN)_6]$ (2.62 g, 8.00 mmol). The reaction mixture was vigorously stirred for 30 min. The precipitated Ni-PBA, $Ni^{II}_3[Fe^{III}(CN)_6]_2{\cdot}13H_2O$, was separated in a procedure similar to that in the case of the insoluble PB NP solid with a yield of 3.13 g (90%), where the hydration number was similarly estimated using TG-DTA.

The insoluble Ni-PBA NP solid (3.19 g, 4.00 mmol as the formula of $Ni^{II}_3[Fe^{III}(CN)_6]_2{\cdot}11H_2O$) was stirred with water (10 mL) for 2 hrs. Into the resulting yellow suspension, an aqueous solution (16.7 ml) of $K_4[Fe(CN)_6]{\cdot}3H_2O$ (0.845 g, 2.00 mmol, 10% based on the total number of metal (Ni and Fe) ions of the Ni-PBA) was added, and the mixture was then stirred for 2 weeks. After the centrifugal removal of aggregated large particles of the Ni-PBA NPs at 2600 × g for 10 min, the ink of Ni-PBA NPs (Ni-PBA NP ink) (148.5 mM as the formula of $Ni^{II}_3[Fe^{III}(CN)_6]_2{\cdot}11H_2O$) was diluted with water to adjust to various concentrations.

Fabrication of single-layer (SL) and double-layer (DL) thin films using PB NP and Ni-PBA NP inks

To fabricate SL films composed of PB NPs or Ni-PBA NPs (Fig. 1b), PB NP (5–60 mM) or Ni-PBA (5–100 mM) NP inks (150 μL) were developed on the plasma-treated hydrophilic surface of an ITO glass substrate (2 × 2 cm^2) using a spin-coating technique (first step: accelerate from 0 to 2000 rpm for 15 sec; second step: 2500 rpm for 5 sec), and spin-coated NP SL films were sintered at a low temperature between 100 and 150 °C for 1 hr in a constant-temperature oven. To prepare DL films of the PB NPs and the Ni-PBA NPs with different thicknesses, the as-sintered PB NP SL film received a topcoat of the Ni-PBA NP inks with various concentrations *via* a similar spin-coating process, and the hybridised films were further sintered at 100–150 °C for 1 hr.

Electrochemical measurements

The electrochemical properties of SL and DL films of PB and Ni-PBA NPs were investigated in a 0.1-M LiCl, NaCl, or KCl electrolyte aqueous solution controlled at pH 3 by the addition

of a diluted HCl aqueous solution under applied potentials between -0.3 and 1.2 V *vs.* Ag/AgCl using an ALS plate material evaluating cell (measurement area: 47.8 mm^2).

Fabrication of DL film on an ITO PET substrate

An electrochemical measurement area (2 × 2 cm^2) was exposed on an ITO PET substrate (5 × 6 cm^2) while covering the other area with masking tape. A similar DL film composed of the PB NPs and the Ni-PBA NPs was fabricated on the as-masked ITO PET substrate using the same procedures as for the spin-coating and the low-temperature sintering. After removing the masking tape, the electrochemical properties of the as-prepared DL film were investigated using a column-shaped glass cell with a diameter of 25.2 mm (Fig. S12).

Acknowledgements

This work was partially supported by a Grants-in-Aid for Scientific Research (C) (No. 24550069), (B) (No. 15H03783), and Young Scientists (B) (No. 26810030) of the Japan Society for the Promotion of Science (JSPS). This work was funded by the Mukai Science and Technology Foundation.

Notes and references

1 S. Kitagawa. R. Kitaura and S. Noro, *Angew. Chem. Int. Ed.,* 2004, 43, 2334; A. Corma, H. García and F. X. Llabrés i Xamera, *Chem. Rev.*, 2010, **110**, 4606; H. Furukawa, K.E. Cordova, M. O'keeffe and O. M. Yaghi, *Science*, 2013, **341**, 1230444; W. Zhong and R.-G. Xiong, *Chem. Rev.,* 2013, **112**, 1163; A. Carné, C. Carbonell, I. Imaz and D. Maspoch, *Chem. Soc. Rev.,* 2011, **40**, 291; A. Morozan and F. Jaouen, *Energ. Environ. Sci.,* 2012, **5**, 9269; M. D. Allendorf, A. Schwartzberg, V. Stavila and A. A. Talin, *Chem. Eur. J.,* 2011, **17**, 11372.

2 V. Stavila, A. A. Talin and M. D. Allendorf, *Chem. Soc. Rev.,* 2014, **43**, 5994; E. Cornado and G. M. Espallargas, *Chem. Soc. Rev*., 2013, **42**, 1525.

3 A. Kraft, *Bull. Hist. Chem.* 2008, **33**, 61.

4 O. Sato, *J. Photochem. Photobiol. C-Photochem. Rev*., 2004, **5**, 203; R. Lescouëzec, L. M. Toma, J. Vaissermann, M.Verdaguer, F. S. Delgado, C. Ruiz-Pérez, F. Lloret and M. Julve, *Coord. Chem. Rev*., 2005, **249**, 2691; H. Tokoro and S. Ohkoshi, *Dalton trans*., 2011, **40**, 6825; S. Ohkoshi, H. Tokoro and K. Hashimoto, *Coord. Chem. Rev.*, 2005, **249**, 1830; S. Ohkoshi, S. Takano, K. Imoto, M. Yoshikiyo, A. Namai and H. Tokoro, *Nat. Photon.,* 2014, **8**, 65.

5 K. Itaya, T. Ataka and S. Toshima, *J. Am. Chem. Soc.,* 1982, **104**, 4767.

6 V. D. Neff, *J. Electrochem. Soc.,* 1978, **125**, 886; K-C Cheng, F-R Chen and J-J Kai, *Electrochim. Acta*, 2007, **52**, 3330; W. Chen, J. Tang and X.-H. Xia, *J. Phys. Chem. C.,* 2009, **113**, 21577; M. Takachi, T. Matsuda and Y. Moritomo, *Jpn. J. Appl. Phys*., 2013, **52**, 044301.

7 B. Kong, C. Selomulya, G. Zheng and D. Zhao, *Chem. Soc. Rev*., 2015, in press, DOI: 10.1039/c5cs00397k

8 M. Singh, H. M. Haverinen, P. Dhagat and G. E. Jabbour, *Adv. Mater.,* 2010, **22**, 673; R. R. Søndergaard, M. Hösel and F. C. Krebs, *J. Polymer Sci. B Polymer Phys.,* 2013, **51**, 16; H. Minemawari, T. Yamada, H. Matsui, J. Tsutsumi, S. Haas, R. Chiba, R. Kumai and T. Hasegawa, *Nature,* 2011, **475**, 364; P. H. Lau, K. Takei, C. Wang, Y. Ju, J. Kim, Z. Yu, T. Takahashi, G. Cho and A. Javey, *Nano lett.,* 2013, **13**, 3864; T. Someya, T. Sekitani, S. Iba, Y. Kato, H. Kawaguchi and T. Sakurai, *Proc. Natl. Acad. Sci. USA,* 2004, **101**, 9966.

9 K. Fukuda, Y. Takeda, Y. Yoshimura, R. Shiwaku, L. T. Tran, T. Sekine, M. Mizukami, D. Kumaki and S. Tokito, *Nat. comm.,* 2014, **5**, 4147.

10 J. Perelaer, P. J. Smith, D. Mager, D. Soltman, S. K. Volkman, V. Subramanian, J. G. Korvink and U. S. Schubert, *J. Mater. Chem.,* 2010, **20**, 8446.

11 A. Kamyshny, J. Steinke and S. Magdassi, *Open Appl. Phys. J.,* 2011, **4**, 19.

12 J. Perelaer and U. S. Schubert, *J. Mater. Res.,* 2013, **28**, 564.

13 S. Park, G. Wang, B. Cho, Y. Kim, S. Song, Y. Ji, M.-H. Yoon and T. Lee, *Nat. Nano.,* 2012, **7**, 438.

14 M. S. White, M. Kaltenbrunner, E. D. Głowacki, K. Gutnichenko, G. Kettlgruber, I. Graz, S. Aazou, C. Ulbricht, D. A. M. Egbe, M. C. Miron, Z. Major, M. C. Scharber, T. Sekitani, T. Someya, S. Bauer and N. S. Sariciftci, *Nat. Photon.,* 2013, **7**, 811.

15 B. T. Anto, S. Sivaramakrishnan, L.-L. Chua and P. K. H. Ho, *Adv. Funct. Mater.,* 2010, **20**, 296; K. Fukuda, T. Sekine, R. Kobayashi, Y. Takeda, M. Shimizu, N. Yamashita, D. Kumaki, M. Itoh, M. Nagaoka, T. Toda, S. Saito, M. Kurihara, I. Sakamoto and S. Tokito, *Org. Electron*, 2012, **13**, 3296.

16 A. Gotoh, H. Uchida, M. Ishizaki, T. Satoh, S. Kaga, S. Okamoto, M. Ohta, M. Sakamoto, T. Kawamoto, H. Tanaka, M. Tokumoto, S. Hara, H. Shiozaki, M. Yamada, M. Miyake and M. Kurihara, *Nanotechnology,* 2007, **18**, 345609.

17 M. Ishizaki, K. Kanaizuka, M. Abe, Y. Hoshi, M. Sakamoto, T. Kawamoto, H. Tanaka and M. Kurihara, *Green Chem.,* 2012, **14**, 1537.

18 L. Britnell, R. V. Gorbachev, R. Jalil, B. D. Belle, F. Schedin, A. Mishchenko, T. Georgiou, M. I. Katsnelson, L. Eaves, S. V. Morozov, N. M. R. Peres, J. Leist, A. K. Geim, K. S. Novoselov and L. A. Ponomarenko, *Science*, 2012, **335**, 947; N. Huo , J. Kang , Z. Wei , S.-S. Li , J. Li and S.-H. Wei, Adv. Funct. Mater. 2014, **24**, 7025; R. Cheng, D. Li, H. Zhou, C. Wang, A. Yin, S. Jiang, Y. Liu, Y. Chen, Y. Huang and X. Duan, *Nano Lett*., 2014, **14**, 5590; J. Meng, J.-J. Chen, L. Zhang, Y.-Q. Bie, Z.-M. Liao and D.-P. Yu, *Small*, 2015, **11**, 1660; T. Niu and A. Li, *Prog. Surf. Sci*., 2015, **90**, 21; S. Burnside, S. Winkel, K. Brooks, V. Shklover, M. Grätzel, A. Hinsch, R. Kinderman, C. Bradbury, A. Hagfeldt and H. Pettersson, *J. Mater. Sci.-Mater. Electron.* 2000, **11**, 355.

19 H. D. Abruna, P. Denisevich, M. Umana, T. J. Meyer and R. W. Murray, *J. Am. Chem. Soc.,* 1981, **103**, 1; P. Denisevich, K. W. Willman and R. W. Murray, *J. Am. Chem. Soc.,* 1981, **103**, 4727; R. M. Metzger, *Chem. Rev.* 2003, **103**, 3803; C. H. W. Cheng, S. W. Boettcher, D. H. Johnston and M. C. Lonergan, *J. Am. Chem. Soc*., 2004, **126**, 8666; K. Miecznikowski, M. Chojak, W. Steplowska, O. Makowski, P. J. Kulesza, L. Adamczyk, M. A. Malik, M. Gałkowski and H. Bala, *Pol. J. Chem.,* 2004, **78**, 1183.

20 D. M. Pajerowski, T. Watanabe, T. Yamamoto and Y. Einaga, *Phys. Rev. B,* 2011, **83**, 153202.

21 J. C. Wojdeł, I.P.R. Moreira, S. T. Bromley and F. Illas, *J. Mater. Chem.,* 2009, **19**, 2032.

22 A. Takahashi, H. Tanaka, N. Minami, M. Kurihara and T. Kawamoto, *Bull. Chem. Soc. Jpn*., 2015, **88**, 69.

23 E. Reguera, J. Fernández-Bertrán, A. Dago and C. Día, *Hyperfine Interact*., 1992, **73**, 295.

24 V. Panchal, A. Lartsev, A. Manzin, R. Yakimova, A. Tzalenchuk and O. Kazakova, *Sci. Rep.,* 2014, **4**, 5881; C. Joachim, J. K. Gimzewski and A. Aviram, *Nature,* 2000, **408**, 541; W. Lee, K. Kim, W. Jeong, L. A. Zotti, F. Pauly, J. C. Cuevas and P. Reddy, *Nature,* 2013, **498**, 209; J. V. Barth, G. Costantini and K. Kern, *Nature,* 2005, **437**, 671.

25 J. Li, Y. Zhang, S. To, L. You and Y. Sun, *ACS nano,* 2011, **5**, 6661; Y. Z. Long, M. Yu, B. Sun, C. Z. Gu and Z. Fan, *Chem. Soc. Rev.,* 2012, **41**, 4560.

Double-layer films of Prussian blue (PB) and its analogue nanoparticles act as an electron-rectifier controlled by the PB bottom layer with a 20-nm thickness

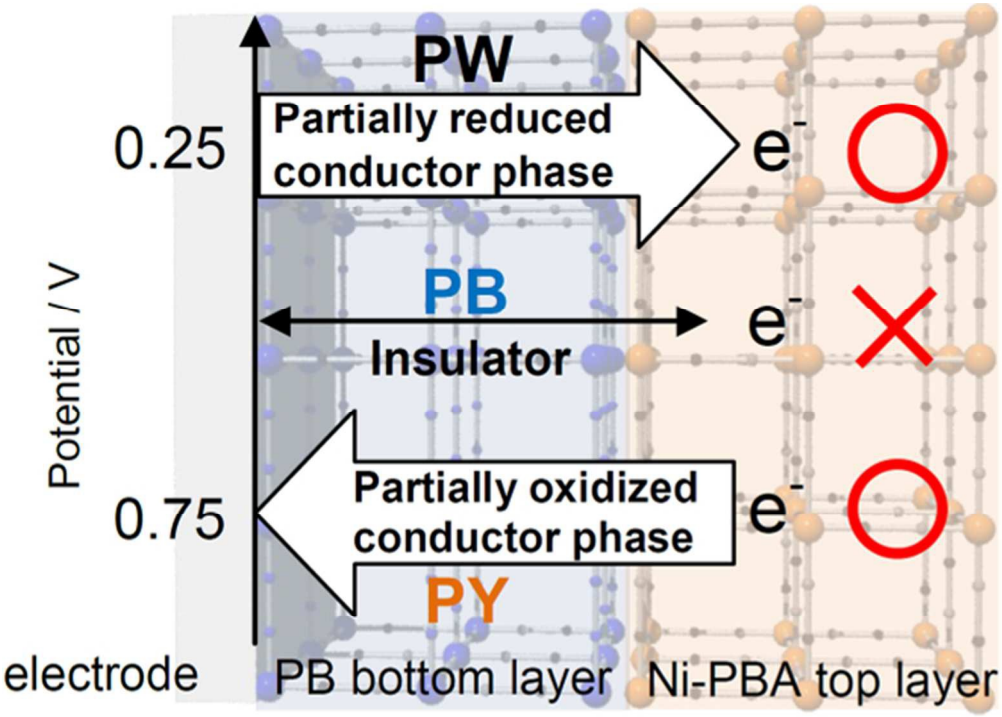

55x39mm (300 x 300 DPI)